Analysis of valence shell electronic excitations in silicon and its refractory compounds using electron energy loss microspectroscopy

W. M. Skiff, R. W. Carpenter, and S. H. Lin

Center for Solid State Science, Arizona State University, Tempe, Arizona 85287-1704

Valence shell electronic excitations in silicon, and its carbide, nitride, and oxide are studied using electron energy loss microspectroscopy in a transmission electron microscope, at 1-eV resolution with a 100-keV electron beam. This so-called "low-loss" region of the spectrum is normalized to scattering cross section per valence electron for each compound, and a large, sequential, variation in the cross section across the series of compounds is reported. The low-loss cross section is calculated using the Born approximation by including single-electron transitions in the target. Both band-to-band and band-to-continuum transitions are included, by using extended Hückel band calculations to obtain the valence shell crystal states, using the electron gas model for the ionization states, and using the random phase approximation to obtain differential cross sections. The calculations yield semiquantitative results, and allow for a chemical interpretation of the experimental results. The relation of the present model to that for plasmon excitation is also briefly discussed.

INTRODUCTION

The current technological effort to develop advanced materials which make use of silicon-based ceramic and electronic materials requires the ability to acquire and interpret structural and spectroscopic information from small regions of such materials. This effort has helped to spawn several recent advances in analytical transmission electron microscopy, including developments in the method of electron energy loss microspectroscopy. This method allows for quantitative elemental and chemical analysis of small microstructural features, such as precipitate particles,[1] whose composition and electronic structure are of interest.[2] The interpretation of such energy loss spectra (ELS) is still in a state of development.

Recently we reported an investigation of the Si L and C, N, and O K core-shell-absorption edges in energy loss spectra taken from single-phase regions of silicon, and its carbide, nitride, and oxide.[3] In this investigation the experimental edge intensities were normalized to scattering cross section per atom, and then were calculated using some semiempirical models.

Briefly, the core-shell-absorption cross section was calculated as a sum of two contributions. The first was that from core shell transitions to tight-binding, crystal, valence shell states above the Fermi level, giving rise to chemically dependent fine structure in the spectral region near the onset of the edge. The second contribution was that from core shell transitions to ionization states (which lie above the vacuum level). These states were taken as outgoing plane waves, to account for elemental effects in the ionization region of the edge, which begins $\simeq 5$–10 eV above the edge onset. The ionization states were then modified by including the elastic backscattering of the outgoing plane waves off the atoms which neighbor the excited atom, to account for the chemically dependent fine structure in the ionization region.

Encouraged by the success of these models, in this paper we apply the same theory to calculate the valence shell absorption cross section in these nonconducting materials, and

compare the results with the cross sections obtained from the experiment.[4] If the models are correct, they should semiquantitatively explain the strong variation in the valence shell absorption cross section among the materials of present interest, shown in Fig. 1, in terms of the chemical variation among these compounds. These appear to be the first reported cross-section calculations for valence shell excitation in insulators by electron impact.

In the following we review the application of the Born approximation and the single-electron transition model to the calculation of the inelastic scattering cross section. The experimental details are then given, and the region of each spectrum corresponding to valence shell excitation, the so-called low-loss region, is normalized to scattering cross section per valence shell electron. The low-loss regions from the four materials can then be compared on an absolute basis. In the next section the cross-section contribution from band–band transitions, that is, from transitions from occupied to unoccupied valence shell crystal states, is calculated using the results of our previous extended Hückel band calculations.[3] The ionization contribution to the low-loss region is then calculated by including transitions from the occupied valence shell crystal states to plane-wave ionization states above the vacuum, ignoring the weaker modification of the ionization final states by the elastic backscattering of the outgoing plane wave by the atoms neighboring the scattering center. A discussion of these results and the theoretical model, as well as some appropriate comments on the relation of the present model to the well-known model for plasmon excitation by electron impact in metals,[4] concludes this paper.

THEORETICAL BACKGROUND

The differential cross section for inelastic scattering of a swift electron with an energy loss E in a direction ω is given by[5]

$$\frac{d^2\sigma(E,\omega)}{dE\,d\omega} = \frac{4}{a_0^2}\frac{q_f}{q_i}\frac{1}{q^4}S(\mathbf{q},E), \qquad (1)$$

where the incident and scattered wave vectors $\mathbf{q}_i$ and $\mathbf{q}_f$, respectively, define the momentum transferred to the target, $\hbar\mathbf{q}$, by $\mathbf{q} = \mathbf{q}_i - \mathbf{q}_f$. S is the dynamical form factor for the scattering event, which can be written in terms of the macroscopic, generalized dielectric constant, ϵ, as[6]

$$S(\mathbf{q},E) = \frac{q^2}{4\pi^2 e^2 C} \, \mathrm{Im}\left(\frac{-1}{\epsilon(\mathbf{q},E)}\right). \qquad (2)$$

$C = N/V$, where N is the number of valence shell electrons in the solid and V is the volume. For the case of a weak interaction between the swift electron and the target, it has been shown that the quantum mechanical expression for ϵ can be written as[7,8]

$$\frac{1}{\epsilon(\mathbf{q},E)} = 1 - \frac{4\pi e^2}{q^2 V} \sum_f \left(\frac{|\langle\Phi_f|\Sigma_j \exp(-i\mathbf{q}\cdot\mathbf{r}_j)|\Phi_i\rangle|^2}{E + E_f - E_i + i\gamma_f} \right.$$
$$\left. - \frac{|\langle\Phi_f|\Sigma_j \exp(i\mathbf{q}\cdot\mathbf{r}_j)|\Phi_i\rangle|^2}{E - E_f + E_i + i\gamma_f} \right), \qquad (3)$$

where Φ_i and Φ_f are the many-electron initial and final state wave functions of the target, with E_i and E_f the corresponding energies, and γ_f is a vanishingly small damping constant. Using the relation

$$1/(x + i\gamma) = P(1/x) - i\pi\delta(x)$$

with Eqs. (3) and (2), S becomes[8]

$$S(\mathbf{q},E) = 1/N \sum_f \left(|\langle\Phi_f|\Sigma_j \exp(i\mathbf{q}\cdot\mathbf{r}_j)|\Phi_i\rangle|^2 \right.$$
$$\times \delta(E - E_f + E_i)$$
$$- |\langle\Phi_f|\Sigma_j\exp(-i\mathbf{q}\cdot\mathbf{r}_j)|\Phi_i\rangle|^2$$
$$\left. \times \delta(E + E_f - E_i) \right), \qquad (4)$$

which is the same result as that obtained using the Born approximation.[5,9]

In the single-electron transition model and for the case of a closed-shell initial state, the many-electron matrix element reduces to a single-electron matrix element,[9] so that

$$\sum_f \left| \langle\Phi_f| \sum_j \exp(i\mathbf{q}\cdot\mathbf{r}_j)|\Phi_i\rangle \right|^2$$
$$= \sum_i \sum_f 2|\langle\psi_f(\mathbf{r})| \exp(i\mathbf{q}\cdot\mathbf{r})|\psi_i(\mathbf{r})\rangle|^2, \qquad (5)$$

where ψ_i and ψ_f are the initial and final state single-electron wave functions involved in the transition. When applying Eq. (5) in the single-electron transition model, E_i and E_f in Eqs. (3) and (4) are replaced with the energies of the respective single-electron states. Neglecting inelastic scattering events in which the swift electron gains energy (i.e., cases for which E is negative), and then taking the initial and final single-electron states as continuous in energy, our final expression for S becomes

$$S(\mathbf{q},E) = 2/N \int\int dE_i \, dE_f \, D(E_i)D(E_f)\delta(E - E_f + E_i)$$
$$\times |\langle\psi_f| \exp(i\mathbf{q}\cdot\mathbf{r})|\psi_i\rangle|^2, \qquad (6)$$

where $D(E_i)$ and $D(E_f)$ are, respectively, the density of initial and final states. To calculate the low-loss region of the spectrum, the limits of the integration over the initial state

energy E_i, are taken from the bottom of the lowest valence band in the target to the Fermi energy, and that over the final state energy E_f, from the Fermi level to the desired upper limit.

To apply Eq. (1) to electron energy loss spectra we evaluate S using Eq. (6) and calculated wave functions and densities of states, and then integrate the differential cross section over the solid angle ω, subtended by the spectrometer collection aperture and over a unit of energy loss E, corresponding to the exit slit of the spectrometer, to obtain the partial cross section $\sigma(E)$. For thin targets and kinematic diffracting conditions the collected inelastically scattered intensity $I(E)$, is related to the partial cross section by $I(E)/I_0 \simeq \sigma(E)Ct$, where I_0 is the total incident intensity and t is the target thickness.

EXPERIMENTAL DETAILS

Electron energy loss spectra were obtained from single-phase regions of silicon, α-SiC, β-Si$_3$N$_4$, and partially amorphized α-quartz, as previously described in detail.[3] Only the most essential experimental details are given here. Spectra were obtained with a Philips EM400 TEM fitted with a field emission gun, and coupled to a Gatan 607 magnetic sector spectrometer. The field emission gun was operated without thermal assistance to improve the energy resolution, at 100 keV, with a 100-Å-diam probe, current in the range of 20–30 nA, and a beam convergence half-angle of 5 mrad. The microscope was operated in diffraction mode, with the circular angle-limiting entrance aperture of the spectrometer centered around the direct beam, with an acceptance half-angle of 10 mrad. A liquid-nitrogen cooled sample stage was used to eliminate carbon contamination on the specimen.

Suitably thin, well-characterized, approximately wedge-shaped single-crystal regions of each sample were tilted into kinematic diffracting conditions, with silicon, the carbide, and the nitride near the [110], [0001], and [111] zone axes, respectively. ELS were collected under these conditions, and then calibrated in energy loss to an accuracy of ± 1 eV, using the zero-loss peak and the π^* peak on the C K edge from amorphous carbon at 284 eV loss. These spectra had an estimated energy resolution of 0.5 eV, based on the FWHM of the zero-loss peak. Multiple scattering was not significant in the spectra, as observed from the absence of second and higher order plasmons in the low-loss region, plasmon to zero-loss peak ratios of less than 0.1, and lack of Kikuchi lines and other dynamical effects in the convergent beam diffraction patterns taken from the regions of interest. Furthermore, surface-mode excitation was not significant in the spectra, as observed from the absence of characteristic surface plasmons at energy losses corresponding to $\simeq 1/\sqrt{2}$ of the energy losses for volume plasmon excitation.[4] Hence, the experimental low-loss spectra shown here are dominated by valence shell excitations in the bulk solids, from single-scattering regions of specimen.

The low-loss regions of the spectra were normalized to scattering cross section per valence shell electron per eV as follows. The background-stripped Si L edges from the spectra, with Si L edge onset at $\simeq 100$ eV loss, were first normal-

6329   J. Appl. Phys., Vol. 64, No. 11, 1 December 1988

Skiff, Carpenter, and Lin   6329

ized to cross section per Si atom, within an $\simeq 20\%$ accuracy using the methods previously described. In this procedure we normalized the Si L edges of the four materials to the same atomic scattering cross section at energy losses $\simeq 200$ eV beyond edge onset, in the ionization region of the edges were chemical effects are weak and elemental effects are dominant, and hence the relative accuracy of the Si L absorption cross sections from the four materials is closer to $\simeq 5\%$. This procedure resulted in low-loss cross sections that were normalized per Si atom, which were then converted to that per valence electron by using the stoichiometry and the number of valence electrons per formula unit for each compound.

The resulting low-loss cross sections are shown in Fig. 1, with the zero-loss peak excluded for clarity. Across the series of compounds, from the silicon to the carbide, nitride, and oxide, notice that the maximum of the plasmon peak steadily increases in energy from $\simeq 17$ to $\simeq 22$ eV loss, that the magnitude of this peak steadily decreases by a factor of $\simeq 4$, and that the broadening of this peak steadily increases. Although other smaller features can be seen in these spectra, it is primarily these gross spectral variations that we want to explain in terms of the chemical variation across this series of compounds.

BAND–BAND CONTRIBUTIONS

To calculate the band–band contributions to the low-loss absorption cross section we make use of the tight-binding LCAO calculations previously reported for silicon, α-SiC, β-Si$_3$N$_4$, and α-quartz, that were used to calculate the near-edge fine structure in the core-shell-absorption edges from these materials.[3] The μth single-electron valence shell crystal states ψ_μ, was taken as a linear combination of Bloch wavefunctions b_j's,

$$\psi_\mu(\mathbf{K},\mathbf{r}) = \sum_A \sum_{j_A} C_{j_A\mu}(\mathbf{K}) b_{j_A}(\mathbf{K},\mathbf{r}), \qquad (7)$$

where A runs over the atoms in the unit cell, and j_A over the valence shell atomic orbitals on atom A, ϕ_{j_A}'s, with the Bloch functions given by[10,11]

$$b_{j_A}(\mathbf{K},\mathbf{r}) = N_c^{-1/2} \sum_{\mathbf{R}} e^{i\mathbf{K}\cdot\mathbf{R}} \phi_{j_A}(\mathbf{r} - \mathbf{R} - \mathbf{r}_A). \qquad (8)$$

$\mathbf{R}$ runs over the N_c unit cells in the crystal, and $\mathbf{r}_A$ points from the cell origin to the A th atom. For each of the Bloch wave vectors $\mathbf{K}$ that were numerically chosen to span the irreducible wedge in reciprocal space,[11] the Bloch wave interactions, $H_{ij} = \langle b_i|\hat{H}|b_j\rangle$, were parametrized to valence shell atomic orbital ionization potentials using the extended Hückel method,[12,13] while summing over first nearest-neighbor interactions. The atomic basis set consisted of Slater-type[14,15] Si 3s, 3p, 3d, 4s, and 4p orbitals, and 2s, 2p, 3s, and 3p orbitals for C, N, and O, with the effective nuclear charges and atomic orbital ionization potentials the same as previously used.[3] The eigenvalue problem,

$$\bar{\bar{H}}(\mathbf{K})\bar{\bar{C}}(\mathbf{K}) = \bar{\bar{C}}(\mathbf{K})\bar{\epsilon}(\mathbf{K}), \qquad (9)$$

was then solved to obtain crystal state energies, ϵ_μ's, and wave functions. For each Bloch wave vector $\mathbf{K}$, the resulting

crystal states were filled in ascending energy with the number of valence shell electrons in the unit cell, to obtain the Fermi level. The density of states,

$$D(E_a) = \left(\frac{L}{2\pi}\right)^3 \sum_\mu \int \delta[E_a - \epsilon_\mu(\mathbf{K})]d\mathbf{K}, \qquad (10)$$

and the projected density of j_A states,

$$\rho_{j_A}(E_a) = \left(\frac{L}{2\pi}\right)^3 \sum_\mu \int |C_{j_A\mu}(\mathbf{K})|^2 \delta[E_a - \epsilon_\mu(\mathbf{K})]d\mathbf{K}, \qquad (11)$$

were then evaluated separately for occupied and unoccupied states. L^3 is the volume of the unit cell, and the integration is over the Brillouin zone.

The band–band scattering cross sections were evaluated using Eqs. (6) and (1), and the crystal wave functions and density of states, as follows. Making use of the approximations,[3] where only single-center integrals in the single-electron matrix elements are retained, neglecting the cross terms when squaring the matrix element in Eq. (6) (the random phase approximation), and then ignoring the variation in the differential cross section for bound–bound atomic transitions over unit energy loss, the band–band contribution to the differential cross section per unit cell becomes

$$\frac{d^2\sigma(E,\omega)}{dE\,d\omega}$$

$$= \sum_A \sum_{i_A} \sum_{j_A} \frac{d\sigma_{i_A,j_A}(E,\omega)}{d\omega}$$

$$\times \int\int \rho_{i_A}(E_i)\rho_{j_A}(E_f)\delta(E - E_f + E_i)dE_i\,dE_f, \qquad (12)$$

with the differential cross section for the bound–bound atomic transitions (i_A–j_A transitions) given by

$$\frac{d\sigma_{i_A,j_A}(E,\omega)}{d\omega} = \frac{8}{a_0^2} \frac{q_f}{q_i} \frac{1}{q^4} |\langle\phi_{j_A}|e^{i\mathbf{q}\cdot\mathbf{r}}|\phi_{i_A}\rangle|^2. \qquad (13)$$

The band–band cross section per valence electron is obtained by dividing Eq. (12) by the number of valence shell electrons in the unit cell. Notice that, in this treatment, the intra- and interband transitions are included simultaneously.

We evaluated the atomic matrix elements in Eq. (13) analytically using the dipole approximation, taking into account the effects of target orientation in the solid state, as follows. We write

$$\langle\phi_j|\exp(i\mathbf{q}\cdot\mathbf{r})|\phi_i\rangle \simeq i\langle\phi_j|q_{x_t}x + q_{y_t}y + q_{z_t}z|\phi_i\rangle, \qquad (14)$$

where q_{x_t}, q_{y_t}, and q_{z_t} are the Cartesian components of $\mathbf{q}$ with respect to the coordinate system of the target t. These components of $\mathbf{q}$ are then written in terms of those relative to a coordinate system with the z axis along $\mathbf{q}_i$, q_{x_i}, q_{y_i}, and q_{z_i}, using the transformation

$$(q_{x_t}q_{y_t}q_{z_t})^T = \bar{\bar{A}}_{t,i}(q_{x_i}q_{y_i}q_{z_i})^T, \qquad (15)$$

which are then substituted into Eq. (14). The Euler angles[16] which define the elements of $\bar{\bar{A}}$ were determined from the analysis of the diffraction pattern. The quantities $\langle\phi_j|x|\phi_i\rangle$, $\langle\phi_j|y|\phi_i\rangle$, and $\langle\phi_j|z|\phi_i\rangle$ were then evaluated analytically

using the same Slater-type orbitals that were used in the band calculations, and using the decomposition relation for the angular part of the integration into Wigner $3j$ coefficients.[15,17] The resulting matrix element in Eq. (14) was substituted into Eq. (13) and squared.

To obtain the band–band partial cross section from Eqs. (12) and (13), the integration over the solid angle subtended by the collection aperture ω, was done analytically for the small-angle scattering case, by using the relations[4]

$$q_{x_i} \simeq -q_i\theta\cos\phi, \quad q_{y_i} \simeq -q_i\theta\sin\phi, \quad q_{z_i} \simeq q_i\theta_E,$$
$$q^2 \simeq q_i^2(\theta^2 + \theta_E^2),$$

and

$$d\omega \simeq \theta\,d\theta\,d\phi, \tag{16}$$

where θ and ϕ are, respectively, the polar and azimuthal scattering angles of $\mathbf{q}_f$ relative to $\mathbf{q}_i$, and $\theta_E = E/(2E_0)$ is the so-called characteristic scattering angle, with E_0 the energy of the incident beam.

The resulting calculated band–band contributions to the low-loss cross section per valence electron were added to the band–continuum contributions (discussed in the next section), and the results are shown in Fig. 1. It is clear that

the band–band transitions dominate the low-loss plasmon peak. Notice that these results semiquantitatively predict the decreasing magnitude of the low-loss cross section, within an $\simeq 30\%$ accuracy, based on the scaling factors given in Fig. 1, and that they qualitatively predict the shift in energy and the increasing broadening of the plasmon peak. Also notice, however, that the calculated peaks at $\simeq 45$ eV loss, as well as other fine details, do not agree well with experiment. The source of these errors will be explained in the final discussion, because our immediate interest is in extracting a physical interpretation from the calculated results.

To interpret the band–band low-loss contributions we actually calculated the respective Si, C, N, and O atom cross-section contributions separately, according to Eq. (12). The magnitudes of the C, N, and O atom contributions were about ten times smaller than those of the Si atom contributions. This was because the largest calculated C, N, and O atomic cross sections, corresponding to the $2s\rightarrow 2p$ and $2p\rightarrow 2s$ transitions, were about an order of magnitude smaller than those for Si atom, corresponding to the $3p\rightarrow 3d$, $3d\rightarrow 3p$, $3s\rightarrow 3p$, and $3p\rightarrow 3s$ transitions. This was true even when we varied the effective nuclear charges in the atomic orbitals around Slater's atomically reasonable values. In oth-
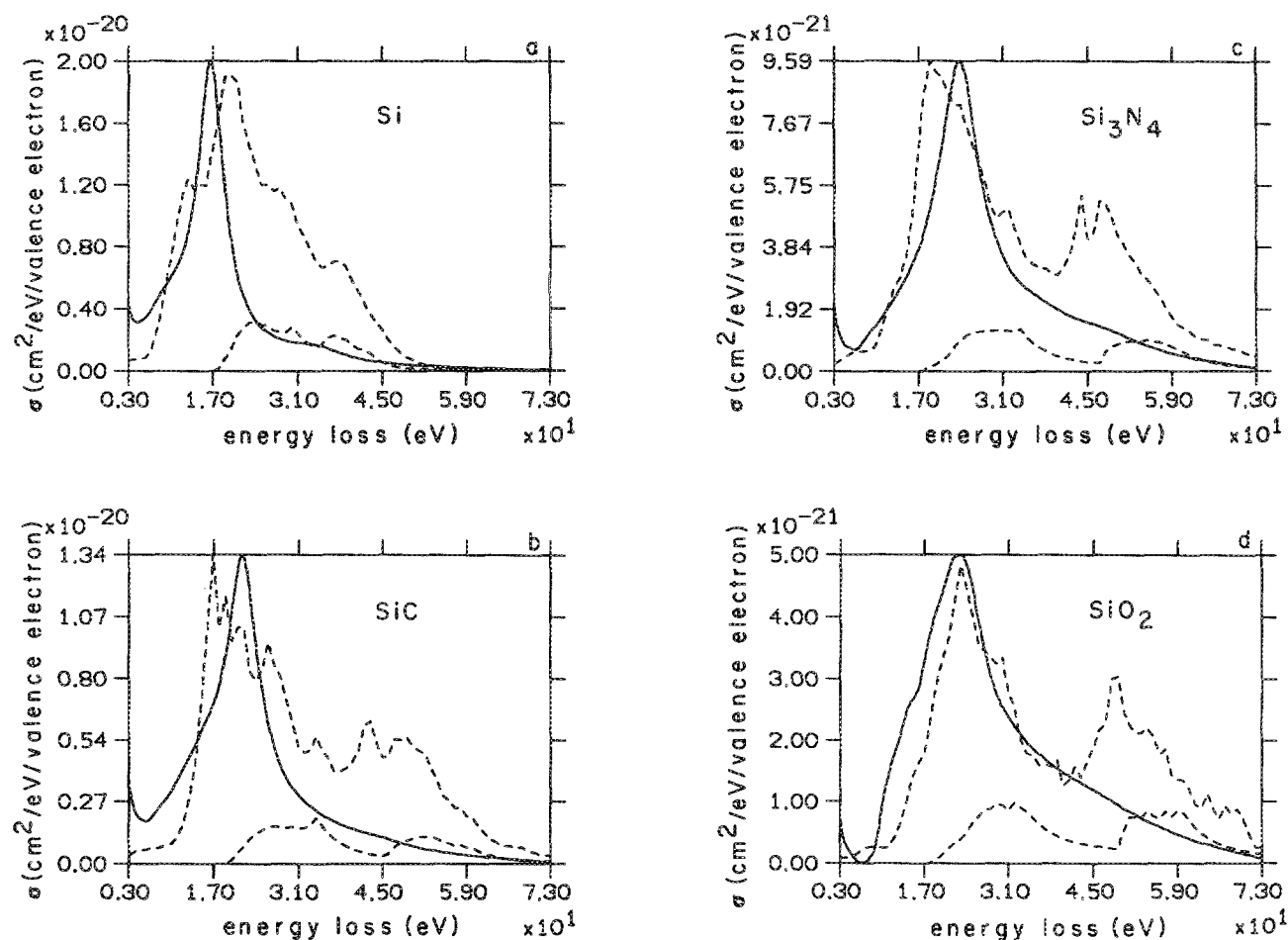

FIG. 1. Experimental valence shell excitation cross sections per valence electron for (a) silicon, (b) α-SiC, (c) β-Si$_3$N$_4$, and (d) α-quartz are shown as solid curves. The zero-loss peak is not shown for clarity. The dashed curve which begins at $\simeq 17$ eV loss is the calculated band–continuum contribution to the low-loss cross section. The other dashed curve is the sum total of the calculated band–band and band–continuum cross-section contributions. (The calculated band–band cross sections were multiplied by 0.6, 0.915, 0.994, and 0.7, respectively, to fit the experimental cross sections.)

er words the valence shell electrons of C, N, and O atoms are more tightly bound than those of Si, and hence have a lower probability of excitation. We conclude that variations in band–band contributions to the low-loss cross sections among these materials can be interpreted largely in terms of variations in the projected densities of Si valence shell atomic orbitals in the occupied and unoccupied crystal states.

An interpretation of this variation in the Si band–band cross-section contribution across this series of compounds can be separated into two effects. First, across this series from the silicon to the oxide, the number of Si atoms per valence electron decreases by a factor of 4, which then reduces the densities of Si atomic orbitals in the crystal valence shell states, and lowers the band–band cross section by about the same amount. This effect reflects changes in elemental composition.

The second effect is a chemical effect which involves the variation in the energy distribution of the densities of the Si atomic orbitals in the occupied and unoccupied crystal states. An inspection of the population analyses of the calculated electronic structures[3] shows that the bonding states for the carbide, nitride, and oxide are split into two regions of bands that are separated by a $\simeq$ 12-eV gap. This gives rise to the calculated bimodal band–band cross sections for these materials as shown, and accounts for some of the increasing broadening of the low-loss cross section across the series.

The population analyses also show that the effects of Si atom oxidation across this series are to transfer some of the population of Si atomic orbitals from the bonding states into the excited states, and also to shift the population in the upper bonding bands to lower energy and that in the lowest unoccupied bands to higher energy. The latter effect gives rise to the shift in energy of the maximum of the band–band cross section, from $\simeq$ 17 to 22 eV loss, as shown. The former population transfer effect does not tend to be visible in the low-loss region, because the joint projected density of initial and final states, as seen in Eq. (12), tends to smear this effect out.

BAND–CONTINUUM CONTRIBUTIONS

The ionization contribution to the valence shell excitation cross section was evaluated by taking the initial state as an occupied, tight-binding valence shell state, the same as above. And the final state was approximated as that for an electron gas, which ignores the effective potential in the effective mass Hamiltonian,[11] corresponding approximately to the ionization state in a bulk solid.[18,3] The final state was, hence, taken as a plane wave, i.e., $\psi_f \propto \exp(i\kappa \cdot r)$, with the wave vector related to the final state energy by the relation $\kappa^2 = 2m^* E_f / \hbar^2$, where E_f is positive and m^* is the effective mass of the ejected target electron. The density of states in a given direction, ω_κ, in the solid was taken as that of an electron gas.[19]

Previously we used this final-state model to calculate analytical expressions for the differential cross section for atomic ionization of hydrogenlike atomic orbitals (with the usual quantum numbers n, l, and m) in a bulk solid,[20] denoted by $d^2\sigma_{n,l,m}(E,\omega)/dE\,d\omega$. In an empirical procedure we introduced a crude phase shift into the plane wave, by

replacing m^* with m in the exponential, which gave reasonable results with respect to experiment. As such the m^* dependence in the differential cross section reduces to a proportionality factor of (m^{*2}), that controls the magnitude of the cross section by acting as a scaling factor. The shape is controlled by the effective nuclear charge in the initial atomic state and by the ionization threshold energy.

In addition we showed that

$$\int d\omega \frac{d^2\sigma_{n,l,m}(E,\omega)}{dE\,d\omega}$$
$$= \frac{1}{2l+1} \int d\omega \frac{d^2\sigma_{n,l}(E,\omega)}{dE\,d\omega}, \qquad (17)$$

for at least the case of small angle scattering with the aperture centered around the direct beam, and independent of target orientation. $d^2\sigma_{n,l}/dE\,d\omega$ is the differential cross section for atomic ionization of the n,l subshell, when the $2l + 1$ magnetic substates are degenerate. This result considerably simplifies the calculation of the ionization contribution to the valence shell absorption cross section.

The band–continuum differential cross section was then evaluated by applying the initial state crystal wave function and density of states given in Eqs. (7) and (10), and the final state ionization wave function and density of states, to the single-electron transition model in Eq. (6). By retaining only single-center integrals in the single-electron matrix element, making the random phase approximation, and then ignoring the variation in the differential cross section for bound–continuum atomic transitions over unit energy loss, the ionization contribution to the differential cross section per unit cell becomes

$$\frac{d^2\sigma(E,\omega)}{dE\,d\omega}$$
$$= \sum_A \sum_{i_A} \frac{d^2\sigma_{(n,l,m)_{i_A}}(E,\omega)}{dE\,d\omega}$$
$$\times \int \int \rho_{i_A}(E_i)\delta(E - E_f + E_i)dE_i\,dE_f, \qquad (18)$$

where the density of final states has been included in the atomic ionization cross section. The index on the atomic ionization cross section, $(n,l,m)_{i_A}$, refers to the n, l, and m quantum numbers of the i_A th atomic orbital of atom A. The band–continuum cross section per valence shell electron is obtained by dividing Eq. (18) by the number of valence electrons in the unit cell.

We evaluated the atomic ionization partial cross sections using Eq. (17), the analytical expressions previously reported,[20] and the same effective nuclear charges for the valence shell atomic orbitals as used in the band calculations.[3] The effective mass for the ejected target electron in the ionization state was taken as $m^*/m = 0.0316$ for the four compounds. This unrealistically low value was chosen to give the best fit to the experimental cross sections, when the ionization and band–band calculated cross sections were added together to obtain the total calculated low-loss cross sections. A more reasonable value of the effective mass would be $m^*/m \simeq 0.1$; we comment on this problem in the discussion.

The resulting calculated band–continuum contributions to the low-loss cross section are shown in Fig. 1. In this case the magnitudes of the C, N, and O ionization contributions were only four to five times smaller than those from Si atoms in the respective compounds, which differs somewhat from the previous band–band results. However, notice that the band–continuum cross sections decrease by a factor of $\simeq 3$ across the series of compounds, that a bimodal cross-section distribution is observed for the carbide, nitride, and oxide, and that the energy of the first maximum shifts from $\simeq 20$ to 26 eV loss. These effects are similar to those observed for the band–band calculated cross sections, and can be explained using the same arguments, with the exception that the variations in the unoccupied valence shell crystal states are not involved. The onsets of the calculated ionization cross section are at $\simeq 17$ eV loss in the four materials, which corresponds to the fact that the calculated Fermi levels were $\simeq -17$ eV with respect to vacuum. Also notice that the maxima in the ionization contributions tend to overlap with the minima in the band–band contributions, producing an overall broadening effect across the series of compounds.

DISCUSSION

The source of most of the error in the present calculation is in the Hückel parametrization used in the band calculation, and the choice of the potential for the ionization state in the bulk. Self-consistent field band calculations, such as with a CNDO/2 parametrization,[21] should yield more accurate crystal wave functions, projected densities of states, crystal state energies with respect to vacuum and each other, and an overall better result in both the shape and magnitude of the calculated low-loss region. It is clear that this region is extremely sensitive to the valence shell electronic structure. We also expect that the inclusion of a potential in the Hamiltonian for the ionization state will effect the magnitude and the shape of the ionization cross sections, and a more reasonable value of the effective mass for the ejected target electron (closer to $m^*/m \simeq 0.1$) should result. The elastic backscattering of the outgoing ionization plane waves by the atoms that neighbor the excited atom (extended fine structure),[3,22,23] and the coupling between the unbound (positive energy) valence shell states and the continuum[24] should also have a noticeable effect on the present result.[3] We believe that these improvements must first be included in the present calculation, before the limitations of the single-electron transition model can be quantitatively evaluated. We note that the breakdown of the single-electron transition model itself necessarily involves many-body effects in the many-electron matrix elements of Eqs. (3) and (4). For example, relaxation of the final many-electron state can give rise to excitonic effects.

A rather curious feature in the low-loss region is the excitation of two plasmons by a single-scattering event.[25,26] Ashley and Ritchie treated the case of an electron-gas metal. They obtained an expression for the double-plasmon scattering probability by including the Coulombic interactions between the electrons in the metal as a perturbation to the

usual electron-gas Hamiltonian.[25] Note that the present calculation implicitly includes the interactions between the electrons in the solid, albeit through the Hückel parametrization, and that it predicts that band–band transitions, from the lowest energy bonding bands, can contribute to peaks that lie at approximately double the plasmon energy loss. Unfortunately the error in the present band calculation prevents us from concluding whether or not this is fortuitous. Batson and Silcox have recently reported highly accurate experimental measurements of the low-loss cross section in aluminum, as a function of scattering angle and energy loss, and were thus able to distinguish between various types of excitations, by first carefully recovering the single-scattering spectrum from the experimental data.[26] Such exacting experiments need to be done for the silicon compounds studied here, and the results compared with more accurate theory.

It is appropriate to briefly comment on the relationship of the present model to the well-known model for plasmon excitation in metals. To do this we refer to the pioneering work of Ritchie,[27] and then clarify one point. Ritchie derived an expression for the differential scattering probability per unit thickness, $C d^2\sigma(E,\omega)/dE\, d\omega$, which can also be obtained using Eqs. (1) and (2), and then obtained an approximate expression for the differential scattering probability in a free-electron metal, using Lindhard's expression for the generalized dielectric constant of an electron gas. Lindhard's expression[28] for $\epsilon(q,E)$ can be obtained by treating both the occupied and unoccupied valence shell states as plane waves, with the zero point energy taken at the bottom of the lowest valence band, and then evaluating Eq. (3) using the single-electron transition model according to Eq. (5). We give this derivation in the Appendix, where it is shown that the "collective" aspect of the plasmon excitation for this electron-gas model is a direct result of the summations over initial and final single-electron target states, and is not a many-body effect in the transition matrix element. The present model is then essentially an extension of this earlier single-electron transition model, with the electron-gas description of the electronic structure of the solid replaced with an LCAO description.

Finally, it is interesting to compare the electron-gas model with the present LCAO model for the valence shell electronic structure. The former predicts a plasmon energy E_p of 16.6, 23.1, 24.7, and 24.2 eV, respectively, for silicon, and its carbide, nitride, and oxide. These values fit closely with the experimental ones. In fact, the calculated low-loss cross section for silicon, using the electron-gas model, agrees very well with the experiment.[4] Frankly, it is difficult to reconcile these results with the present LCAO model. However, in principle, one should be able to perform an accurate band calculation for a metal, and then expand the resulting wave functions in Fourier series, and recover the electron gas model. To our knowledge this useful calculation has not yet been reported.

Physical insight into the LCAO molecular orbital (MO) theory can be obtained by considering a simple system of two atomic orbitals (AOs), ϕ_1 and ϕ_2, centered on two atoms that are separated by a distance R. Solving for the MO energies and wave functions gives[15,29]

$$E_{\pm} = (H_{11} + H_{22} \pm \sqrt{A})/2,$$

$$\psi_{\pm} = \{[1 \pm (H_{11} - H_{22})/\sqrt{A}\,]H_{12}/2|H_{12}|\}^{1/2}\,\phi_1$$

$$\pm \{[1 \pm (H_{22} - H_{11})/\sqrt{A}\,]H_{21}/2|H_{12}|\}^{1/2}\,\phi_2,$$
$$(19)$$

where $A = 4|H_{12}|^2 + (H_{22} - H_{11})^2$ and $H_{ij} = \langle \phi_i | \hat{H} | \phi_j \rangle$. $-H_{ii}$ corresponds roughly to the ionization potential of the ith AO. H_{ij} is the interaction energy of orbital i with j. In the extended Hückel treatment H_{ij} is proportional to $H_{ii} + H_{jj}$ and to the overlap of the AOs, $\langle \phi_i | \phi_j \rangle$, which increases with smaller R. Across the present series of compounds the nearest-neighbor bond lengths steadily decrease (2.35, 1.89, 1.73, and 1.62 Å, respectively), and for Si, C, N, and O atoms, the valence orbital ionization potentials steadily increase. It follows that across the series of compounds the energy of the transition, $E_+ - E_- = \sqrt{A}$, steadily increases.

Further, these effects give rise to the charge transfer effects discussed previously, as can be seen by inspection of the MO wave functions in Eq. (19). However, it should be noted that the LCAO model is incapable of rigorously describing the covalent bond, where $H_{11} = H_{22}$, because ionic contributions to the corresponding many-electron determinantal wave functions are predicted by the model.[15] (The alternative Heitler–London treatment of chemical valence correctly describes the bonding states of a covalent molecule, but cannot correctly predict excited states.[15]) This fundamental limitation of the LCAO model may be responsible for some of the error in the present silicon calculation.

Even with these limitations, the present model for the low-loss region of the energy loss spectrum, which combines band–band and band–continuum transitions in the single-electron transition model, is consistent with earlier work, and it allows for a semiquantitative interpretation of low-loss spectra from the present materials, in terms of elemental composition and electronic structure. Further, this model allows for a similar interpretation of core shell absorption edges in these materials.[3] This approach should be valid for metals and ionic solids, as well as insulators.

ACKNOWLEDGMENTS

APPENDIX

We derive the generalized dielectric constant for the electron-gas metal, starting from Eq. (3) and by applying the single-electron transition model, to obtain the well-known expression for plasmon excitation. Our purpose is to show the origin of the plasmon resonance.

The initial and final state wave functions are taken as Slater determinants of N noninteracting single-particle plane waves, with the initial state a closed shell, i.e., a singlet state. It follows that only singlet–singlet transitions can be

nonzero, and the many-electron matrix element reduces to a single electron-matrix element as given in Eq. (5). In the single-electron transition model Eq. (3) becomes

$$\varepsilon(\mathbf{q},E) = 1 + \frac{2mE_p^2}{N\hbar^2 q^2} \sum_i \sum_f \frac{|\langle \psi_f | \exp(-i\mathbf{q}\cdot\mathbf{r}) | \psi_i \rangle|^2}{E + E_f - E_i + i\gamma}$$
$$- \frac{|\langle \psi_f | \exp(i\mathbf{q}\cdot\mathbf{r}) | \psi_i \rangle|^2}{E - E_f + E_i + i\gamma}, \qquad (A1)$$

where we have used the relation $1/(1 - x) \simeq 1 + x$, and where the plasmon energy E_p is given by $E_p^2 = \hbar^2 4\pi C e^2/m$. $C = N/V$, where N is the number of valence electrons in the solid and V is the volume of the solid.

The single-electron matrix elements are evaluated by the taking the single-electron initial and final state wave functions, respectively, as plane waves, i.e.,

$$\psi_i(\mathbf{r}) = V^{-1/2}\,e^{i\kappa_i \cdot \mathbf{r}}, \quad \psi_f(\mathbf{r}) = V^{-1/2}\,e^{i\kappa_f \cdot \mathbf{r}}, \qquad (A2)$$

at respective energies $E_i = (\hbar \kappa_i)^2/2m$ and $E_f = (\hbar \kappa_f)^2/2m$. The single-electron matrix elements are then evaluated for $V \to \infty$, e.g.,

$$\langle \psi_f | \exp(-i\mathbf{q}\cdot\mathbf{r}) | \psi_i \rangle = (2\pi)^3/V \quad \delta(-\kappa_f - \mathbf{q} + \kappa_i). \qquad (A3)$$

Because of these delta functions the quantity $E_f - E_i$ in the first and second terms inside the summations in Eq. (A1) becomes, respectively,

$$E_f - E_i = (\kappa_f^2 - \kappa_i^2)\hbar^2/2m = [(\kappa_i - \mathbf{q})^2 - \kappa_i^2]\hbar^2/2m$$

and

$$E_f - E_i = (\kappa_f^2 - \kappa_i^2)\hbar^2/2m = [(\kappa_i + \mathbf{q})^2 - \kappa_i^2]\hbar^2/2m, \qquad (A4)$$

so that the summation over final states, from the Fermi level to infinity, can be done immediately, by replacing the summation with a volume integration, i.e.,

$$\sum_f \to \int D(\kappa_f)d\kappa_f = \frac{V}{(2\pi)^3}\int d\kappa_f. \qquad (A5)$$

Applying the relation, $f(\mathbf{r}) = \int f(\mathbf{r}')\delta(\mathbf{r} - \mathbf{r}')d\mathbf{r}'$, and the integral representation of the delta function gives

$$\int d\kappa_f \delta(-\kappa_f + \mathbf{q} + \kappa_i)^2$$
$$= \delta(0)$$
$$= \frac{1}{(2\pi)^3}\int \exp(i0.\mathbf{r})d\mathbf{r}$$
$$= V/(2\pi)^3, \qquad (A6)$$

for $V \to \infty$. Equation (A1) then reduces to Lindhard's result,[28]

$$\varepsilon(\mathbf{q},E) = 1 + \frac{2mE_p^2}{N\hbar^2 q^2}\sum_i \frac{1}{E + (q^2 - 2\mathbf{q}.\kappa_i)\hbar^2/2m + i\gamma}$$
$$- \frac{1}{E - (q^2 + 2\mathbf{q}.\kappa_i)\hbar^2/2m + i\gamma}. \qquad (A7)$$

The two terms inside the summation are then combined using the relation $1/(a + b) - 1/(a - b) = -2b/(a^2 - b^2)$, and the result is expanded up to order $1/E^4$, using the relation $1/(1 + x) \simeq 1 - x + x^2$. ε becomes

$$\varepsilon(\mathbf{q},E) \simeq 1 - (2E_p^2/NE^2)\sum_i 1 - \{(2/E)(-\mathbf{q}.\kappa_i\hbar^2/m + i\gamma) + (1/E^2)[(\mathbf{q}.\kappa_i\hbar^2/m)^2 - 2i\gamma\mathbf{q}.\kappa_i\hbar^2/m - \hbar^4 q^4/4m^2]\}$$

$$+ [(2/E)(-\mathbf{q}.\kappa_i\hbar^2/m + i\gamma) + O(1/E^2)]^2 + O(1/E^3). \qquad (A8)$$

The summation over initial states, from zero (at the bottom of the valence band) to the Fermi level, is replaced with integration, for which three types of integrals are evaluated in spherical coordinates:

$$\frac{N}{2} = \sum_i = \int D(\kappa_i)d\kappa_i = [V/(2\pi)^2]\,2\kappa_F^3/3, \qquad (A9)$$

$$\sum_i \mathbf{q}.\kappa_i = \int D(\kappa_i)\mathbf{q}.\kappa_i d\kappa_i = 0, \qquad (A10)$$

$$\sum_i (\mathbf{q}.\kappa_i)^2 = \int D(\kappa_i)(\mathbf{q}.\kappa_i)^2 d\kappa_i$$
$$= [V/(2\pi)^2]2q^2\kappa_F^5/15. \qquad (A11)$$

Ritchie's expression for the dielectric constant is recovered[27]:

$$\varepsilon(\mathbf{q},E) = 1 - (E_p^2/E^2)[(1+\delta) - 2i\gamma/E],$$

with

$$\delta = (\hbar^4/m^2E^2)(q^4/4 + 3q^2\kappa_F^2/5). \qquad (A12)$$

Substituting $\mathrm{Im}(-1/\varepsilon) = \mathrm{Im}\,\varepsilon/(\mathrm{Re}^2\,\varepsilon + \mathrm{Im}^2\,\varepsilon)$ into Eqs. (2) and (1) gives

$$\frac{d^2\sigma}{dE\,d\omega} = \frac{1}{a_0^2\pi^2 e^2 Cq^2}\frac{2\gamma EE_p^2}{[E^2 - E_p^2(1+\delta)]^2 + (2\gamma E_p^2/E)^2}, \qquad (A13)$$

with the resonance occurring when

$$E^2 \simeq E_p^2 + (q^4/4 + 3q^2\kappa_F^2/5)\hbar^4/m^2. \qquad (A14)$$

Notice that the plasmon resonance in this electron-gas model arises from the summations over initial and final states, and not from many-body effects in the matrix element as is commonly assumed. This resonance is completely within the generality of the single-electron transition model.

[1]W. M. Skiff, H. L. Tsai, and R. W. Carpenter, Mater. Res. Soc. Symp. Proc. **59**, 241 (1986).

[2]J. Silcox, in *Introduction to Analytical Electron Microscopy*, edited by J. J. Hren, J. I. Goldstein, and D. C. Joy (Plenum, New York, 1979), Chap. 10, pp. 295–304.

[3]W. M. Skiff, R. W. Carpenter, and S. H. Lin, J. Appl. Phys. **62**, 2439 (1987).

[4]A recent review on this topic is given by H. Raether, in *Springer Tracts in Modern Physics*, edited by G. Höhler (Springer, Berlin, 1980), Vol. 88.

[5]H. A. Bethe, Ann. Phys. **5**, 325 (Leipzig, 1930).

[6]D. Pines, in *Elementary Excitations in Solids* (Benjamin, New York, 1964), Chap. 3, pp. 56–167.

[7]P. Nozières and D. Pines, Nuovo Cimento **9**, 470 (1958).

[8]R. Brout and P. Carruthers, *Lectures on the Many-Electron Problem* (Wiley/Interscience, New York, 1963), pp. 127–138.

[9]S. H. Lin, Proc. R. Soc. (London) A **335**, 51 (1973).

[10]F. Bloch, Z. Phys. **52**, 555 (1928).

[11]J. Callaway, *Energy Band Theory* (Academic, New York, 1964), pp. 1–46, 102–108, 233–244.

[12]M. Wolfsberg and L. Helmholz, J. Chem. Phys. **20**, 837 (1952).

[13]R. Hoffmann, J. Chem. Phys. **39**, 1397 (1963).

[14]J. C. Slater, Phys. Rev. **36**, 57 (1930).

[15]H. Eyring, J. Walter, and G. E. Kimball, *Quantum Chemistry* (Wiley, New York, 1944), pp. 80–91, 162–163, 209, 212–231.

[16]H. Goldstein, *Classical Mechanics*, 2nd ed. (Addison-Wesley, Reading, MA, 1981), pp. 145–148.

[17]A. Messiah, *Quantum Mechanics*, Vol. I (Wiley, New York, 1961), p. 495, Vol. II (1962), p. 1057.

[18]J. J. Ritsko, S. E. Schnatterly, and P. C. Gibbons, Phys. Rev. Lett. **32**, 671 (1974).

[19]S. H. Lin, Y. Fujimura, H. J. Neusser, and E. W. Schlag, *Multiphoton Spectroscopy of Molecules* (Academic, New York, 1984), pp. 67–68, 223–225.

[20]W. M. Skiff, R. W. Carpenter, S. H. Lin, and A. Higgs, Ultramicroscopy **25**, 47 (1988).

[21]J. A. Pople and D. L. Beveridge, *Approximate Molecular Orbital Theory* (McGraw-Hill, New York, 1970), pp. 75–79.

[22]T. Shiraiwa, T. Ishimura, and M. Sawada, J. Phys. Soc. Jpn. **13**, 847 (1958).

[23]D. E. Sayers, F. W. Lytle, and E. A. Stern, in *Advances in X-Ray Analysis*, edited by B. L. Henke, J. B. Newkirk, and G. R. Mallet (Plenum, New York, 1970), Vol. 13, p. 248.

[24]A. Boeglin, B. Fain, and S. H. Lin, J. Chem. Phys. **84**, 4838 (1986).

[25]J. C. Ashley and R. H. Ritchie, Phys. Status Solidi **38**, 425 (1970).

[26]P. E. Batson and J. Silcox, Phys. Rev. B **27**, 5224 (1983).

[27]R. H. Ritchie, Phys. Rev. **106**, 874 (1957).

[28]J. Lindhard, K. Dan. Vidensk. Selsk. Mater. Fys. Medd. **28** (8), 28 (1954).

[29]L. D. Landau and E. M. Lifshitz, *Quantum Mechanics* (Addison-Wesley, Reading, MA, 1965), pp. 133–136.